# Intricate phase diagram of a prevalent visual circuit reveals universal dynamics, phase transitions, and resonances

Matthew S. Caudill,* Sebastian F. Brandt, Zohar Nussinov, and Ralf Wessel
*Department of Physics, Washington University, Campus Box 1105, St. Louis, Missouri 63130-4899, USA*
(Received 19 March 2009; revised manuscript received 2 September 2009; published 25 November 2009)

Neural feedback-triads consisting of two feedback loops with a nonreciprocal lateral connection from one loop to the other are ubiquitous in the brain. We show analytically that the dynamics of this network topology are determined by algebraic combinations of its five synaptic weights. Exploration of network activity over the parameter space demonstrates the importance of the nonreciprocal lateral connection and reveals intricate behavior involving continuous transitions between qualitatively different activity states. In addition, we show that the response to periodic inputs is narrowly tuned around a center frequency determined by the effective synaptic parameters.

DOI: 10.1103/PhysRevE.80.051923 PACS number(s): 87.18.Sn, 84.35.+i, 87.19.lj, 87.19.lt

Neural microcircuits are well-defined networks of neurons with connectivity patterns exquisitely adapted for performing specific signal-processing tasks [1–3]. One prevalent connectivity pattern found among neural microcircuits consists of two feedback loops with a nonreciprocal lateral connection from one loop to the other (Fig. 1). We refer to this topology as a feedback triad. In mammalian visual pathways for instance, this topology forms one of many microcircuits that are linked by poorly isolated cortico-cortico interactions [Fig. 1(a)] [4–6]. In contrast, the isthmic visual pathway of birds and reptiles [Fig. 1(b)] maintains the synaptic topology of the feedback-triad but is more-isolated from other brain areas [7–11]. Therefore the visual circuit of birds and reptiles offers a substrate to investigate the functional significance of the isolated feedback triad.

In this paper, we address the fundamental question of how synaptic weights influence the dynamics and signal-processing characteristics of a single feedback-triad microcircuit. We show that the network's dynamics are not controlled by individual synaptic weights but rather by algebraic combinations of them that crucially depend upon the nonreciprocal lateral connection for the generation of complex network activity. We further show that these algebraic combinations determine the center frequency of the resonance profile of the network. The insights gained into how synaptic weights control a network's dynamics and signal-processing carry fundamental implications for our understanding of neural development, neuromodulation of network activity, and animal-to-animal variability of synaptic parameters.

The feedback-triad microcircuit [Fig. 1(c)] consists of three neurons with one input and five synaptic connections with delays $\tau$. For simplicity, we chose a discrete-time recurrent neural network with a piecewise-linear activation function [12–14] for the representation of the triad circuitry. Specifically, the activity $x_i$ of neuron $i$ at time $t$ depends upon the activities $x_j$ of coupled neurons $j$ at the earlier time $t-\tau$ according to the following equations of motion:

$$x_i(t) = \sigma\left(\sum_{j=1}^{3} w_{ij}x_j(t-\tau) + s_i\right). \tag{1}$$

The matrix $w_{ij}$ measures the strength of connections between neurons $i$ and $j$ and the nonlinear transfer function $\sigma$ is chosen to be the max function $\sigma(u)=\max\{0,u\}$ $u \in \Re$, guaranteeing nonnegative neuronal activities. Based on the circuit connectivity shown in Fig. 1(c), the synaptic weight matrix is given by

$$w = \begin{pmatrix} 0 & \beta & \alpha \\ b & 0 & c \\ a & 0 & 0 \end{pmatrix}, \tag{2}$$

where the feed-forward connections are denoted by Latin letters and the recurrent connections by Greek letters. To

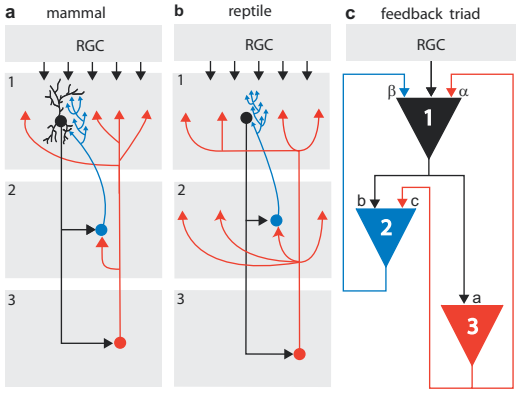


FIG. 1. (Color) Neural feedback triads. (a) In mammals, retinal ganglion cell (RGC) axons (black arrows) project to the thalamic lateral geniculate nucleus (1); this in turn projects to the thalamic reticular nucleus (2) and to the cortex (3). The latter two nuclei feed back to the lateral geniculate nucleus (1). (Modified after [5].) (b) In reptiles, RGC axons project to the optic tectum (1); this in turn projects to the nucleus isthmi pars parvocellularis (2) and to the nucleus isthmi pars magnocellularis (3). The latter two nuclei feed back to the optic tectum (1). (Modified after [10].) Note the nonreciprocal lateral connection from (3) to (2) in each circuit. (c) The feedback triad consists of two feedback loops with a nonreciprocal lateral connection between them.

*mcaudill@physics.wustl.edu

 

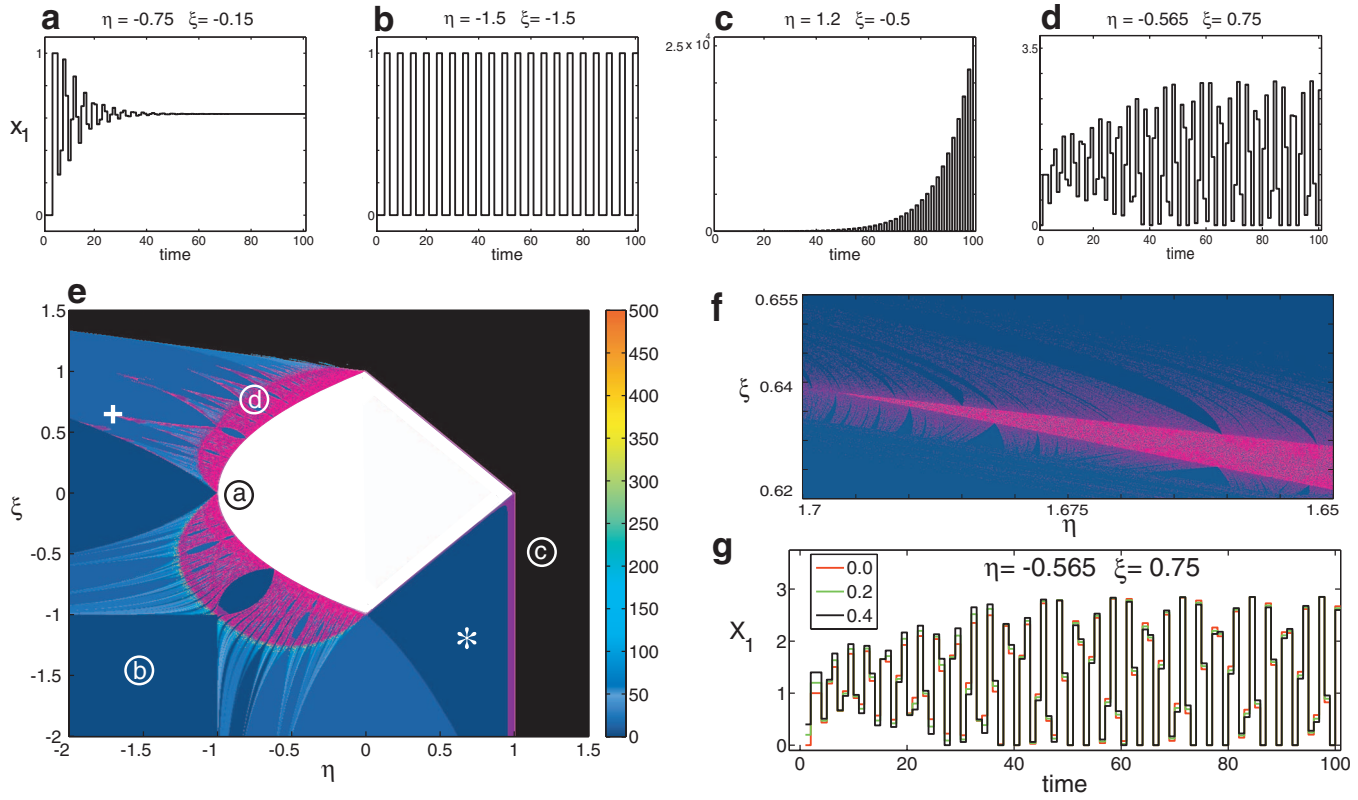


FIG. 2. (Color) Dynamics of feedback-triads. Subfigures (a)–(d) show converging, oscillatory, diverging, and quasiperiodic activity states that result from choosing different combinations of the two effective synaptic parameters $\eta$ and $\xi$. Subfigure (e) shows the color coded parameter space of activities. The white region corresponds to stable fixed points, the black region to unstable fixed points, the blue to orange colors represent oscillations with periods corresponding to the color and the cyan represents quasiperiodic states. Lastly, the purple region represents long period oscillations not represented on the color bar. (f) Zoom centered on the cross hair indicating a critical region where two Arnol'd tongues overlap and a fractal of the structure appears. (g) Coexistence of multiple attractors (multistability) at one combination of $\eta$ and $\xi$ accessed by different initial conditions.

simplify the analysis, we set the synaptic delays $\tau$ to the same value. Lastly, the input $\boldsymbol{s}$ is given by $(s_1,0,0)$ where $s_1$ is the input from the RGC axons.

We investigate the case in which the feed-forward weights $a$ and $b$ are positive because this assignment has been experimentally established in the vertebrate visual system [15]. In addition, our initial analysis will assume that the weight of the lateral connection $c$ is also positive. Thus, the activities of neurons 2 and 3 will always be positive, and passage of the neuronal input through the nonlinear transfer function is unnecessary for these neurons. With this simplification, Eq. (1) can be reduced from three equations to the following $3\tau$-cycle difference map for the activity of the network, taken as the activity of neuron 1.

$$x_1(t) = \sigma[s_1 + \eta x_1(t-2\tau) + \xi x_1(t-3\tau)]. \tag{3}$$

The synaptic weights now appear only in the combinations

$$\eta = \beta b + \alpha a, \quad \xi = \beta a c, \tag{4}$$

thereby reducing the complexity of the model from five synaptic parameters to two effective synaptic parameters.

In the case of instantaneous signal transfer (i.e., $\tau=0$) the network activity is stationary for all parameter values $\eta$ and $\xi$. However, for nonzero delay the dynamical behavior can be complex and is qualitatively independent of $\tau$ since Eq. (3) can be rescaled in time. Thus we identify the delay with a unit time step and choose the network input $s_1=1$.

By varying the effective synaptic parameters four types of dynamical behaviors emerge, namely, convergent [Fig. 2(a)], oscillatory [Fig. 2(b)], divergent [Fig. 2(c)], and quasiperiodic [Fig. 2(d)]. Color coding these four activity states, a dynamical phase diagram representing network activity numerically in the $\eta$-$\xi$ phase plane has been obtained [Figs. 2(e) and 2(f)]. This parameter space features qualitatively different activity-state regions with fascinating geometrical boundaries. One immediate result is that if the synapse $c$ is zero, the parameter $\xi$ vanishes leaving only converging and period-4 oscillations [Fig. 2(e)] as the biologically relevant activity states. Thus, the nonreciprocal connection between the feedback loops is crucial for generating complex network activity patterns.

The boundaries of the converging region are obtained by substituting a solution of the form $x_1(t)=\lambda^t$ into the linearized form of Eq. (3). This yields one real and a complex-conjugate pair solution. By demanding that the moduli of these eigenvalues be less than one, we determine the boundaries of the fixed-point region to be $\eta^2=\xi^2-1$, $\xi=\eta-1$, and $\xi=1-\eta$ which is consistent with differential-delay-equation models studied previously [16].

The limit-cycle regions in the phase diagram are a result of the nonlinearity imposed on the activity of each neuron by the transfer function $\sigma$. To understand the geometrical boundaries of these regions, we developed a set of constraint equations from our numerical simulation of the steady-state trajectories of activities for each neuron. In particular, the activities of each neuron can be represented by a vector whose length $T$ is the period of the limit cycle. Elements from different vectors are related to each other by Eq. (1) thus giving $3T$ constraint equations. When solved simultaneously these equations yield polynomials in $\eta$ and $\xi$ that form the boundaries of each limit-cycle region.

The striations in the phase diagram are composed of distorted triangular regions of limit-cycle activity known as Arnol'd tongues [20,21]. We solved the corresponding constraint equations for each tongue and found that the boundaries of the largest tongues are described by the following geometric polynomials:

$$\sum_{i=1}^{p} i\eta\xi^{i-1} + \sum_{i=1}^{2p} \xi^{i} = 0 \tag{5a}$$

and

$$1 + \eta\left(\sum_{i=1}^{p} i\eta\xi^{i-1} + \sum_{i=1}^{2p} \xi^{i}\right) = 0. \tag{5b}$$

The upper bound of summation $p$ is the order of the polynomial and is related to the period of the tongue by the equation $p=(T-1)/3$.

Where the tongues are narrow, quasiperiodic activity states [cyan in Fig. 2(e)] separate individual tongues. The quasiperiodic trajectories have irrational periods meaning the trajectory never completes a closed orbit [Fig. 2(d)]. As the magnitude of the parameters $\eta$ and $\xi$ increases the tongues widen until a critical value is reached where individual tongues overlap and the set of quasiperiodic states shrinks to measure zero. At this critical value a fractal of the Arnol'd tongue structure appears [Fig. 2(f)] and the boundaries exhibit chaoticlike dynamics as slight changes in the initial conditions result in drastically different network activity.

We further tested the quasiperiodic activity states for chaotic dynamics by varying the initial conditions and checking whether neighboring trajectories diverged from one another. The trajectories are not chaotic, but they do exhibit qualitatively different activity depending upon the initial conditions [Fig. 2(g)]. This coexistence of multiple attractors is referred to as multistability and has been proposed as a mechanism for memory storage and pattern recognition [17,18].

The parameter space has many regions in which small changes in the effective synaptic weights can lead to qualitatively different network activity states. To understand the transition from one activity state to another, we employed an order parameter $M$ involving the Fourier transform of the network activity. This was motivated by the observation that the Fourier transform of the activity near a regional boundary contained Fourier components consistent with periods corresponding to that region and the adjacent region [Figs. 3(a) and 3(b)]. The order parameter $M=1-\Sigma_{k'\neq k_{\max}} I_{k'}/\Sigma_k I_k$ compares the power $I_k$ of each peak $k$ in the Fourier transform relative to the total power of the spectrum. As the boundary separating the period-2 [star in Fig. 2(e)] and period-6 activity states is crossed, a pronounced phase transition occurs [Fig. 3(c)], indicating that points along the boundaries separating different network states will be acutely sensitive to the initial network activity. To quantify this critical behavior, we determined numerically the network activity for various initial conditions [Fig. 3(d)] and measured the length of the transitory time $\theta$ before the network settles into steady-state activity [Fig. 3(e)]. The results show that the boundaries are multistable, a feature that allows the circuit to show activity-dependent responses, such as are observed experimentally in the mammalian visual system [19].

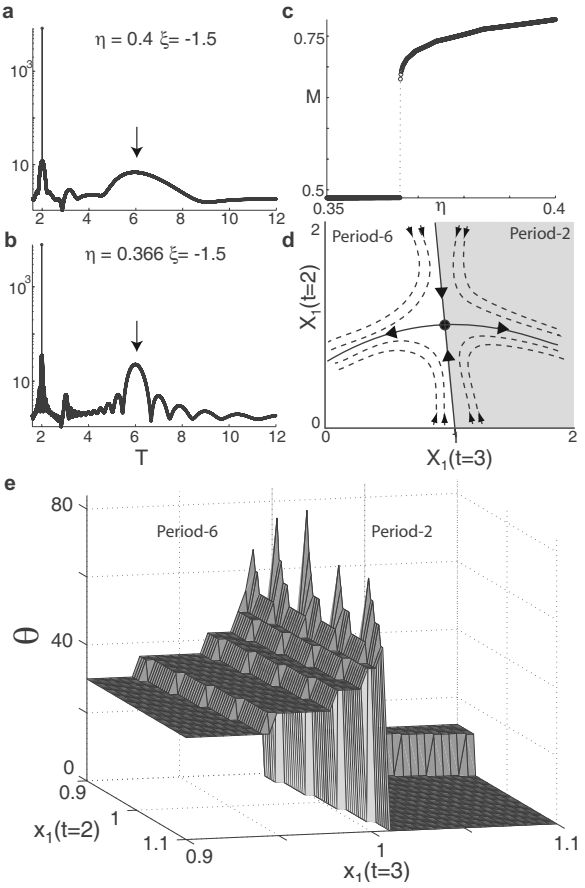


FIG. 3. Critical behavior near the boundary separating the period-2 and period-6 activity states. Plots (a) and (b) show the gathering of Fourier weights around period-6 as the path moves closer to the transition boundary. (c) Order parameter $M$ measured along this path. (d) Phase-space plot depicting activity responses for different $x_1$ initial conditions for a point on the boundary. (e) Transitory time $\theta$ measured near the critical value in the initial conditions.

An important signal-processing characteristic is the susceptibility of the feedback-triad to periodic inputs with specific driving frequencies $\omega$. In Fourier space, the linear response $\tilde{r}(\omega)$ of the triad is related to the stimulus $\tilde{s}(\omega)$ by $\tilde{r}(\omega)=\tilde{\chi}(\omega)\tilde{s}(\omega)$, where $\tilde{\chi}(\omega)$ is the ac susceptibility. This relationship holds for sufficiently weak driving input. For example, at the point $(\eta,\xi)=(-1.5,-1.5)$, the *neural suscepti-*

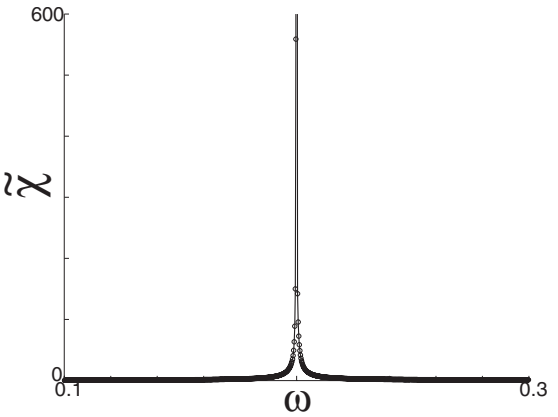


FIG. 4. Susceptibility profile of the feedback-triad over frequencies given in units of $\tau^{-1}$. The susceptibility is sharply tuned about a resonant frequency determined by the two effective synaptic weights. See text and Eq. (6).

*bility* profile was found to follow a scaled Lorentzian of the form

$$\tilde{\chi} = b\left\{\frac{(\Gamma/2)}{\pi[(\Gamma/2)^2 + (\omega - \omega_0)^2]}\right\}, \tag{6}$$

where the Lorentzian width $\Gamma = 2.5 \times 10^{-4}$, the scale factor $b = 0.727\,25$, and the Lorentzian *neural resonant frequency* $\omega_0 = 0.2$. Throughout this work, we set the time step $\tau$ to unity. For a general time step $\tau$, the values of both $b$ and $\omega_0$ quoted above are in units of $\tau^{-1}$. This sharp tuning (Fig. 4) provides an effective bandpass filter that enables the extraction of a specific frequency from the input stimulus. Furthermore, since the resonant frequency depends on the values of the synaptic weights, neuromodulatory substances would allow the microcircuit to switch modes of preferred stimulus frequency.

Our analysis of the feedback triad has been limited by the condition that the nonreciprocal lateral connection between the feedback loops is positive. However, in the mammalian and isthmotectal visual systems the lateral connection $c$ is negative. With this assumption Eq. (1) can be reduced to the following two equations of motion:

$$x_1(t) = \sigma[s_1 + x_2(t - \tau) + \rho x_1(t - 2\tau)], \tag{7}$$

$$x_1(t) = \sigma[\phi x_1(t - \tau) + \psi x_1(t - 2\tau)]. \tag{8}$$

The synaptic weights now appear only in the combinations $\rho = \alpha a/\beta$, $\phi = b/\beta$, and $\psi = ac/\beta$, where we have used the fact that the local feedback connection $\beta$ is positive in the mammalian and isthmotectal visual systems.

Proceeding as before, we identify the delay with a unit time step and choose the network input $s_1 = 1$. By varying the three effective synaptic parameters a three-dimensional parameter space for the activity of neuron $x_1$ has been obtained and visualized in a set of slices through the parameter space (Fig. 5). Although the outline of the unstable fixed points (divergent trajectories) is similar in each slice, the internal structure of both the stable (convergent trajectories) and limit-cycle regions undergo significant changes as the parameter $\phi$ is varied. For sufficiently large values of $\phi$ the parameter space reduces to the two-dimensional model in the parameters $\eta$ and $\xi$ because Eq. (8) no longer requires rectification and can be substituted into Eq. (7).

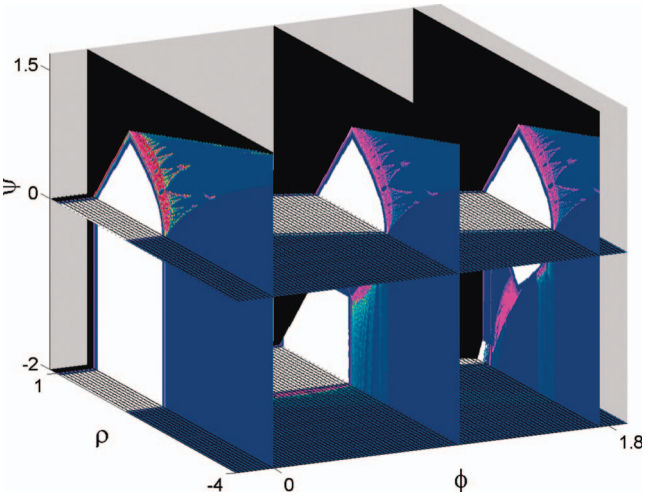


FIG. 5. (Color) Dynamics of feedback triads including negative nonreciprocal lateral connections. Slices at $\phi = (0, 1.5, 1.7)$ through the three-dimensional parameter space defined by the effective synaptic parameters $\rho$, $\phi$, and $\psi$ are shown with the same color-coding as in Fig. 2(e).

Numerous neural and biochemical [22,23] networks can be mapped onto the feedback-triad network topology we have investigated. This study illustrates how complex dynamics can be achieved from very small collections of interacting elements. Specifically, it has been shown that the dynamics and signal-processing characteristics of the feedback triad are determined by two or three combinations of the synaptic weights that depend upon the lateral connection for the generation of complex dynamics. The implications of this study are fourfold. First, the seeming incongruity in animal-to-animal variability of synaptic weights and equivalent dynamics is addressed because network activity is not determined by individual synapses but rather by certain combinations of the synaptic weights. This result is in agreement with previous studies that have shown equivalent dynamics from disparate synaptic weights [24]. Second, manipulation of individual synapses by biochemical agents must likewise be envisioned in terms of combinations of synaptic weights. Third, the existence of continuous transitions between different activity states in the two-dimensional parameter space highlights the flexibility of the dynamics in terms of neuromodulation of the synaptic weights and activity-dependent responses. Last, the signal response is sharply tuned around a center frequency determined by the two effective synaptic weights, indicating that larger networks composed of feedback-triad microcircuits may be suited to bandpass filtering of neural stimuli.

We thank A. Carlsson and J. W. Clark for critical reading of the paper. This work was supported by NIH-EY 15678 and NIH-EY 18818.

[1] G. M. Shepherd, *The Synaptic Organization of the Brain* (Oxford University Press, New York, 2004).
[2] R. Cabeza and A. Kingstone, *Handbook of Functional Neuroimaging of Cognition* (MIT Press, Cambridge, 2006).
[3] S. Grillner and A. Graybiel, *Microcircuits: The Interface Between Neurons and Global Brain Function* (MIT Press, Cambridge, 2006).
[4] S. M. Sherman and R. W. Guillery, *Exploring the Thalamus and Its Role in Cortical Function* (MIT Press, Cambridge, 2006).
[5] A. M. Sillito, J. Cudeiro, and H. E. Jones, Trends Neurosci. **29**, 307 (2006).
[6] R. J. Douglas and K. A. C. Martin, Annu. Rev. Neurosci. **27**, 419 (2004).
[7] E. R. Gruberg, E. A. Dudkin, Y. Wang, G. Marin, C. Salas, E. Sentis, J. C. Letelier, J. Mpodozis, J. Malpeli, H. Cui *et al.*, J. Neurosci. **26**, 10368 (2006).
[8] Y. Wang, D. E. Major, and H. J. Karten, J. Comp. Neurol. **469**, 275 (2004).
[9] Y. Wang, H. Luksch, N. Brecha, and H. Karten, J. Comp. Neurol. **494**, 7 (2006).
[10] M. I. Sereno and P. S. Ulinski, J. Comp. Neurol. **261**, 319 (1987).
[11] A. S. Powers and A. Reiner, Brain Behav. Evol. **41**, 326 (1993).
[12] A. C. Tsoi and A. Back, Neurocomputing **15**, 183 (1997).
[13] Z. Yi and K. K. Tan, IEEE Trans. Neural Netw. **15**, 329 (2004).
[14] R. Haschke and J. Steil, Neurocomputing **64**, 25 (2005).
[15] S. M. Sherman and R. W. Guillery, Philos. Trans. R. Soc. London, Ser. B **357**, 1695 (2002).
[16] J. Bélair and S. Dofour, Can. Appl. Math. Q. **4**, 135 (1996).
[17] C. C. Canavier, D. A. Baxter, J. W. Clark, and J. H. Byrne, J. Neurophysiol. **69**, 2252 (1993).
[18] H. R. Wilson and J. D. Cowan, Biophys. J. **12**, 1 (1972).
[19] M. Steriade, *The Intact and Sliced Brain* (MIT Press, Cambridge, 2006).
[20] V. I. Arnol'd, *Mathematical Methods of Classical Mechanics* (Springer, New York, 1974).
[21] M. H. Jensen, P. Bak, and T. Bohr, Phys. Rev. A **30**, 1960 (1984).
[22] U. Alon, *An Introduction to Systems Biology: Design Principles of Biological Circuits* (CRC, Boca Raton, 2006).
[23] J. A. Papin, J. L. Reed, and B. O. Palsson, Trends Biochem. Sci. **29**, 641 (2004).
[24] A. A. Prinz, D. Bucher, and E. Marder, Nat. Neurosci. **7**, 1345 (2004).